

# The Solar Probe ANalyzer -Ions on Parker Solar Probe

Roberto Livi<sup>1</sup>, Davin E Larson<sup>1</sup>, Justin C Kasper<sup>2</sup>, Robert Abiad<sup>1</sup>, Anthony W Case<sup>3</sup>, Kristopher G Klein<sup>2</sup>, David W Curtis<sup>1</sup>, Gregory Dalton<sup>1</sup>, Michael Stevens<sup>3</sup>, Kelly E Korreck<sup>3</sup>, George Ho<sup>4</sup>, Miles Robinson<sup>1</sup>, Chris Tiu<sup>5</sup>, Phyllis L Whittlesey<sup>1</sup>, J L Verniero<sup>1</sup>, Jasper Halekas<sup>6</sup>, James Mcfadden<sup>1</sup>, Mario Marckwordt<sup>1</sup>, Amanda Slagle<sup>1</sup>, Mamuda Abatcha<sup>1</sup>, and Ali Rahmati<sup>1</sup>

<sup>1</sup>University of California

<sup>2</sup>University of Michigan

<sup>3</sup>Smithsonian Astrophysical Observatory

<sup>4</sup>Applied Physics Laboratory, Johns Hopkins University

<sup>5</sup>NASA

<sup>6</sup>University of Iowa

November 22, 2022

## Abstract

The Solar Probe ANalyzer for Ions (SPAN-I) onboard NASA's Parker Solar Probe (PSP) spacecraft is an electrostatic analyzer with time-of-flight capabilities that measures the ion composition and three dimensional distribution function of the thermal corona and solar wind plasma. SPAN-I measures the energy per charge of ions in the solar wind from 2 eV to 30 keV with a field-of-view of 247.5 \* x 120 \* while simultaneously separating H + from He ++ to develop 3D distribution functions of individual ion species. These observations, combined with reduced distribution functions measured by the Sun-pointed Solar Probe Cup (SPC), will help us further our understanding of the solar wind acceleration and formation, the heating of the corona, and the acceleration of particles in the inner heliosphere. This paper describes the instrument hardware, including several innovative improvements over previous time-of-flight (TOF) sensors, the data products generated by the experiment, and the ground calibrations of the sensor.

## The Solar Probe ANalyzer - Ions on Parker Solar Probe

2 ROBERTO LIVI,<sup>1</sup> DAVIN E. LARSON,<sup>1</sup> JUSTIN C. KASPER,<sup>2,3</sup> ROBERT ABIAD,<sup>1</sup> A. W. CASE,<sup>3</sup> KRISTOPHER G. KLEIN,<sup>4</sup>  
3 DAVID W. CURTIS,<sup>1</sup> GREGORY DALTON,<sup>1</sup> MICHAEL STEVENS,<sup>3</sup> KELLY E. KORRECK,<sup>3</sup> GEORGE HO,<sup>5</sup> MILES ROBINSON,<sup>1</sup>  
4 CHRIS TIU,<sup>6</sup> PHYLLIS L. WHITTLESEY,<sup>1</sup> J. L. VERNIERO,<sup>1</sup> JASPER HALEKAS,<sup>7</sup> JAMES MCFADDEN,<sup>1</sup> MARIO MARCKWORDT,<sup>1</sup>  
5 AMANDA SLAGLE,<sup>1</sup> MAMUDA ABATCHA,<sup>1</sup> AND ALI RAHMATI<sup>1</sup>

6 <sup>1</sup>*University of California, Berkeley, CA, USA*

7 <sup>2</sup>*University of Michigan, Ann Arbor, MI, USA*

8 <sup>3</sup>*Smithsonian Astrophysical Observatory, Cambridge, MA, USA*

9 <sup>4</sup>*Lunar and Planetary Laboratory, University of Arizona, Tucson, AZ 85721, USA*

10 <sup>5</sup>*Applied Physics Laboratory, Laurel, MD, USA*

11 <sup>6</sup>*Heliophysics Science Division, NASA, Goddard Space Flight Center, Greenbelt, MD 20771, USA*

12 <sup>7</sup>*Department of Physics and Astronomy, University of Iowa, Iowa City, Iowa, USA*

13 Submitted to ApJ

### 14 ABSTRACT

15 The Solar Probe ANalyzer for Ions (SPAN-I) onboard NASA's Parker Solar Probe (PSP) spacecraft  
16 is an electrostatic analyzer with time-of-flight capabilities that measures the ion composition and three  
17 dimensional distribution function of the thermal corona and solar wind plasma. SPAN-I measures the  
18 energy per charge of ions in the solar wind from 2 eV to 30 keV with a field-of-view of 247.5° x 120° while  
19 simultaneously separating H<sup>+</sup> from He<sup>++</sup> to develop 3D distribution functions of individual ion species.  
20 These observations, combined with reduced distribution functions measured by the Sun-pointed Solar  
21 Probe Cup (SPC), will help us further our understanding of the solar wind acceleration and formation,  
22 the heating of the corona, and the acceleration of particles in the inner heliosphere. This paper  
23 describes the instrument hardware, including several innovative improvements over previous time-of-  
24 flight (TOF) sensors, the data products generated by the experiment, and the ground calibrations of  
25 the sensor.

26 *Keywords:* plasmas, space vehicles: instruments, solar wind, Sun: corona

### 27 1. INTRODUCTION

28 Parker Solar Probe (PSP) is a robotic NASA mis-  
29 sion designed to make the closest ever in-situ measure-  
30 ments of the Sun. The three-axis stabilized spacecraft  
31 will orbit the Sun with an initial aphelion slightly in-  
32 side Earth's orbit. Through several Venus gravity assists  
33 PSP will decrease its perihelion from 35 solar radii ( $R_s$ )  
34 to 9.68  $R_s$  using a total of 24 orbits within a seven year  
35 time frame. Data collection is configured such that the  
36 primary, high cadence measurements occur during clos-  
37 est approach (10-15 day span), while the remaining time  
38 is spent in cruise phase with a low measurement cadence.  
39 The mission objectives are summarized by the follow-

40 ing three core components: (1) Determine the structure  
41 and dynamics of the magnetic fields at the sources of  
42 the fast and slow solar wind, (2) trace the flow of en-  
43 ergy that heats the solar corona and accelerates the solar  
44 wind, and (3) explore mechanisms that accelerate and  
45 transport solar energetic particles. Further information  
46 on the scientific goals and measurements can be found  
47 in Fox et al. (2016). The SPAN-I instrument is part  
48 of a larger ensemble of plasma sensors called the "So-  
49 lar Wind Electrons, Alphas, and Protons" (SWEAP)  
50 investigation. SWEAP consists of two electron electro-  
51 static analyzers (ESA) (SPAN-E) (Whittlesey 2020, in-  
52 press), one ion ESA (SPAN-I), and a Faraday cup (SPC)  
53 (Kasper et al. 2015) (Case 2019, inpress).

54 SWEAP is designed to characterize the phase space  
55 distribution functions of the solar wind and coronal plas-  
56 mas with the greatest possible completeness and detail

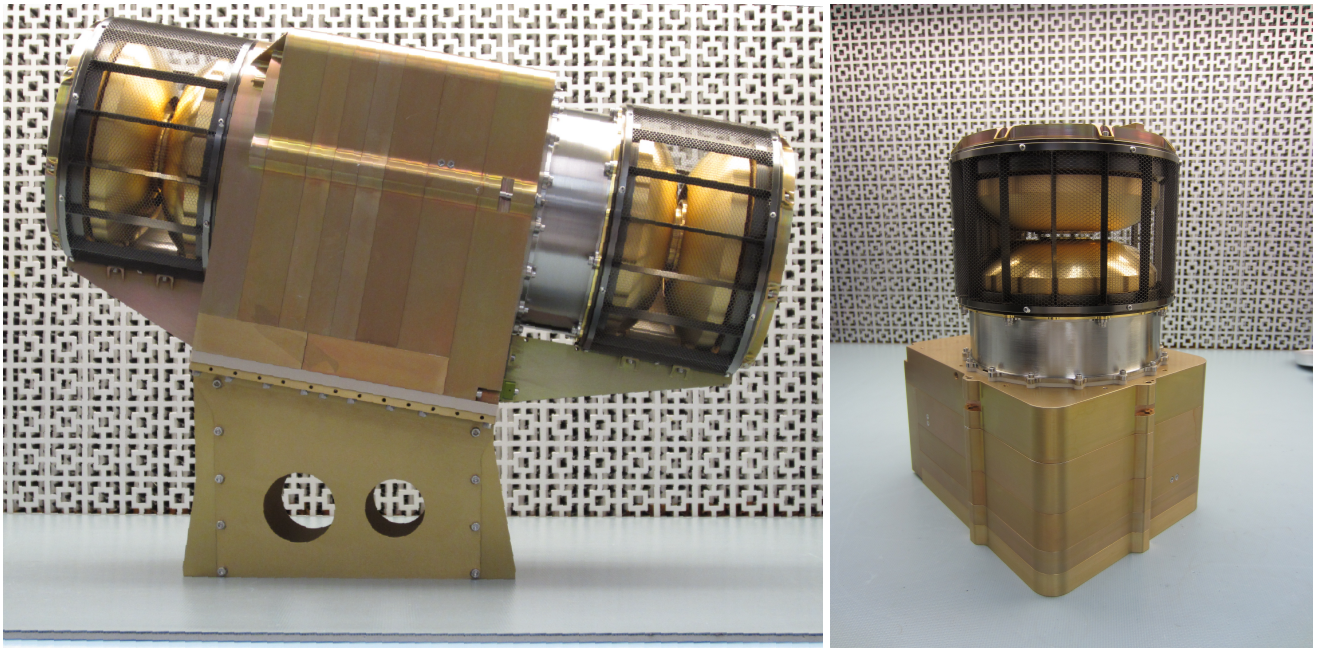


**Figure 1.** Left: SPAN-A Flight Module with the right (SPAN-I) and left (SPAN-E) ESA. SPAN-I consists of an ESA with deflectors followed by a titanium time-of-flight (TOF) section for mass per charge discrimination. Right: SPAN-I separated from the main SPAN-A unit.

57 within modern technological ability. Completeness is  
 58 driven by the desire to observe and distinguish the large  
 59 scale structures and solar wind conditions in all regimes  
 60 of the PSP encounters. Given a continuous record of the  
 61 plasma conditions on each orbit from SWEAP, one seeks  
 62 to study the evolution and interaction of co-rotating solar  
 63 wind streams, the propagation of transients, and more  
 64 broadly the connection from the corona through the inner  
 65 heliosphere. This course of study is key to closure for  
 66 mission objectives (1) and (3), and the SWEAP  
 67 contribution compliments those of all four instrument  
 68 suites. Detail is driven by the desire to measure the  
 69 plasma microstate and spatiotemporal fluctuations that  
 70 signify the wave-particle and kinetic processes governing  
 71 energy transport. These are the keys to the solar wind  
 72 heating and acceleration problem described in mission  
 73 objective (2) of Fox et al. (2016).

74 The SPAN and SPC instruments are designed to be  
 75 complimentary to one another with respect to phase  
 76 space coverage. The SPC instrument, which faces the  
 77 sun and measures charged particle fluxes within a  $\sim 30^\circ$   
 78 field-of-view, is optimized for measurement of positive  
 79 ions in the outer phases of the encounter where solar  
 80 wind flows are primarily radial in the spacecraft frame.  
 81 The SPAN instruments are designed to measure ions  
 82 and electrons beyond that FOV. SPAN-Ion is optimized  
 83 for ion observations near closest approach, where the in-  
 84 flow may be strongly non-radial in the co-moving frame

85 due to the extremely high orbital speed of the space-  
 86 craft which can/will be as high as 190 km/s.

87 The SPAN-A sensor is mounted towards the bottom  
 88 of the spacecraft bus and behind the thermal protection  
 89 shield (TPS). Figure 2 shows the mounting configura-  
 90 tion of the instrument relative to the spacecraft bus and  
 91 the resulting field-of-view. SPAN-A is mounted with a  
 92  $20^\circ$  rotation around the spacecraft z-axis. The FOV plot  
 93 on the right shows the spacecraft in red and the SPAN-  
 94 I small and large anodes along phi and the deflection  
 95 angles along theta. As expected, there is a partial cov-  
 96 erage of anode 0 due to the TPS and the fully extended  
 97 ( $90^\circ$ ) solar panels. The result is that a partial mea-  
 98 surement is made of the true ion flux, which is an aspect  
 99 that will have to be studied and calibrated with inflight  
 100 data. This obstruction is not true for all anode 0 mea-  
 101 surements since there are deflection angles that point  
 102 away from the sun line.

## 103 2. THE ION SOLAR PROBE ANALYZER

104 The SPAN-Ion instrument uses an ESA and a time-of-  
 105 flight (TOF) mass discriminator to resolve ambient ions  
 106 by their incident angle, energy per charge, and mass  
 107 per charge (see figure 1). SPAN-I is able to separately  
 108 resolve the 3D distribution functions of  $H^+$  and  $He^{++}$ ,  
 109 and has some additional capability of measuring higher  
 110 mass per charge elements. The dynamic range of the  
 111 instrument is increased by a mechanical attenuator at

112 the analyzer aperture and an electrostatic spoiler that  
 113 reduces the signal within the ESA.

114 As shown in the block diagram of figure 3, ions are first  
 115 selected in elevation angle by the deflecting electrodes  
 116 and are then filtered by energy per charge as they pass  
 117 through the top-hat electrostatic analyzer. Once they  
 118 exit the ESA, ions are further accelerated by -15 kV  
 119 into the TOF analyzer to resolve their respective mass  
 120 per charge by using a START/STOP double coincidence  
 121 measurement. Ions entering the TOF will have an origi-  
 122 nal energy per charge with an additional of 15 keV be-  
 123 fore they encounter a set of carbon foils that generate  
 124 a pair of START and STOP secondary electrons. The  
 125 START electrons are accelerated by the optical design  
 126 toward the inner portion of the TOF and ultimately im-  
 127 pinge on the microchannel plate (MCP) detectors, simi-  
 128 larly for the STOP electrons which originate from the  
 129 STOP foil directly above the MCPs. The short delay (7-  
 130 200 ns) between the START and STOP signals and the  
 131 short transit gap (2 cm) allows for a measurement of the  
 132 post-accelerated particle velocity. The resulting electron  
 133 cloud from the MCP collects on the anode below it and  
 134 passes through a constant fraction discriminator (CFD)  
 135 to make an accurate time measurement, independent of  
 136 pulse amplitude. Then, the signal is transmitted to the  
 137 digital board below the anode board that contains an  
 138 Application-specific integrated circuit (ASIC) to convert  
 139 signals from high-speed time difference to digital values.  
 140 A full block diagram of the electronic components is  
 141 shown in figure 3 followed by a description of the in-  
 142 dividual electronics boards (see figure 4). A summary  
 143 of the instrument performance parameters and design  
 144 characteristics are shown in table 1.

145 SPAN-I draws significant heritage from the STATIC  
 146 sensor on MAVEN, which was designed to measure Mar-  
 147 tian atmospheric ions and the solar wind. The primary  
 148 difference between these instruments lies in the geomet-  
 149 ric factor, which in the case of SPAN-I was reduced in  
 150 order to avoid saturation of the detector near the Sun.  
 151 This was accomplished by decreasing the hemispherical  
 152 gap size and thus reducing the  $\Delta_R/R$ . The concern  
 153 for saturation was also addressed by the addition of an  
 154 electrostatic 'spoiler' (see section below) to further re-  
 155 duce the geometric factor. Lastly, SPAN-I is built to  
 156 measure the solar wind  $H^+$  and  $He^{++}$  composition and  
 157 higher masses such as  $O^{6+}$  and  $Fe^{7+}$  are present they  
 158 may be too tenuous to be resolved. Both SPAN-I and  
 159 STATIC differ from previous TOF mass spectrometers  
 160 due to their smaller design (<3.3 kg), large dynamic  
 161 range in both energy and particle flux, and in its sim-  
 162 plified electronics that do not require floating detectors

163 at the TOF acceleration potential of -15 kV. Details of  
 164 the instrument subsystems are described below.

### 165 2.1. Electrostatic Analyzer

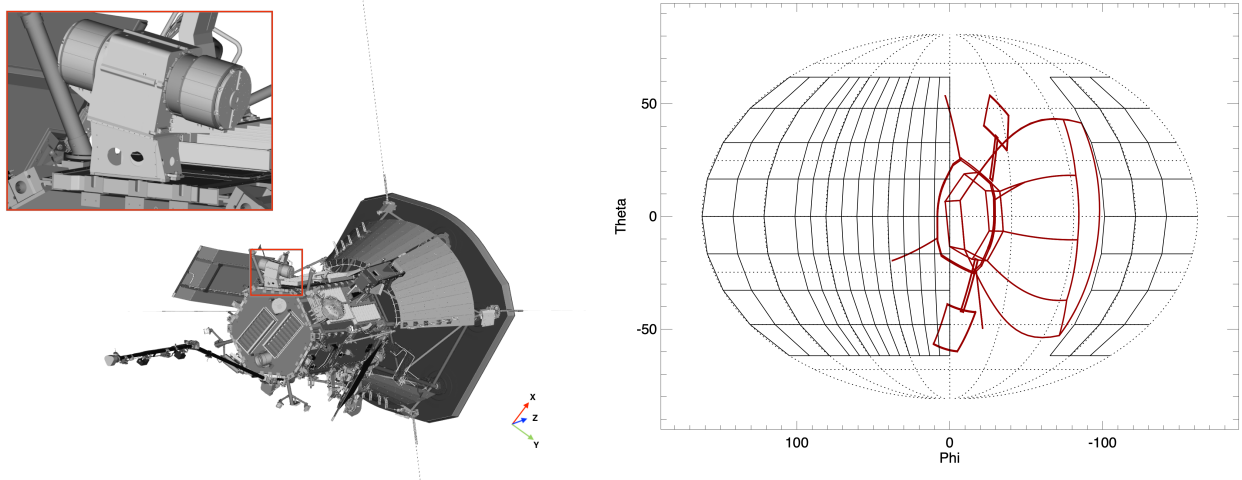
166 SPAN-I's electrostatic analyzer (ESA) geometry  
 167 draws its heritage from the STATIC instrument on  
 168 the MAVEN spacecraft (McFadden et al. 2015). The  
 169 top-hat toroidal approach to ESAs (Carlson et al. 2001)  
 170 used for SPAN-I was originally designed for the Clus-  
 171 ter mission (Reme et al. 1997), and successfully flown  
 172 on the FAST satellite (Klumpar et al. 2001). The ad-  
 173 vantages of the top-hat design are its large geometric  
 174 factor, optimal field-of-view, adequate energy resolution  
 175 (dE/E 7%), and optics that allow exiting ions to be  
 176 properly imaged by subsequent sectors. For SPAN-I,  
 177 the electrostatic focal point is shifted from the exit grid  
 178 of the ESA to the entrance of the -15kV acceleration  
 179 region to optimize the particle throughput within the  
 180 TOF optics. The ESA's outer hemisphere is held at  
 181 ground while the inner section is biased up to -4 kV,  
 182 which provides an energy range between 125 eV and 20  
 183 keV for the first encounters. UV sunlight contamination  
 184 and particle scattering off of the outer surface is reduced  
 185 with the addition of Ebanol-C coating and scalloping  
 186 features. Since the exit of the ESA is close to the -15  
 187 kV HV acceleration sector, it is necessary to add a pair  
 188 of grids at the exit of the ESA in order to reduce fringe  
 189 fields.

### 190 2.2. Electrostatic Deflectors

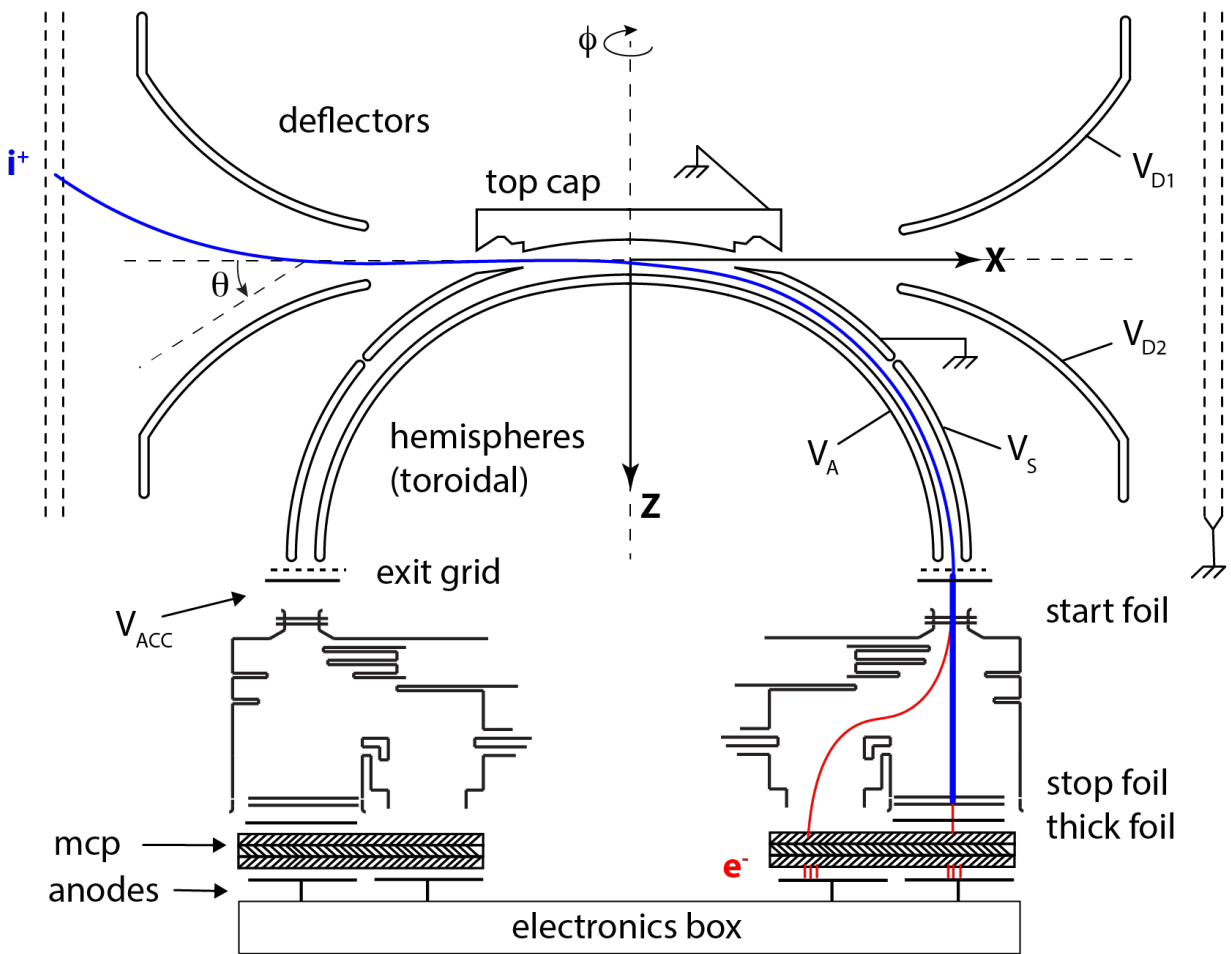
191 In front of the ESA aperture are two deflectors that al-  
 192 low the elevation angle of the instrument to be increased  
 193 by up to +/- 60° at energies as high as 4 keV.

### 194 2.3. Attenuators

195 SPAN-I is capable of measuring a large dynamic range  
 196 of particle fluxes in the solar wind by using two modes  
 197 of attenuation: a mechanical attenuator and an electro-  
 198 static spoiler. The mechanical attenuator is mounted  
 199 between the deflectors and the ESA aperature. Before  
 200 and during launch, the attenuator remains in a closed  
 201 position, together with the one-shot TiNi cover, to pre-  
 202 vent detector contamination and acoustic damage to the  
 203 carbon foils. After launch, the cover is opened and the  
 204 mechanical attenuator is allowed to move the multi-slit  
 205 metal shield in and out of the ESA FOV by using a  
 206 series of nano-muscle shape-memory alloy (SMA) actu-  
 207 ators. The slits allow a reduction in ion fluxes by a factor  
 208 of 10. In addition to the mechanical attenuator, SPAN-I  
 209 includes an electrostatic spoiler, serving as an additional  
 210 electrode that forms the lower half of the outer hemi-  
 211 sphere (the upper half is maintained at ground). When



**Figure 2.** Left: Parker Solar Probe spacecraft with the SPAN-A sensor highlighted in the red box. Right: Mollweide projection of the SPAN-I field-of-view, including partial obstruction of the spacecraft and its TPS (red).



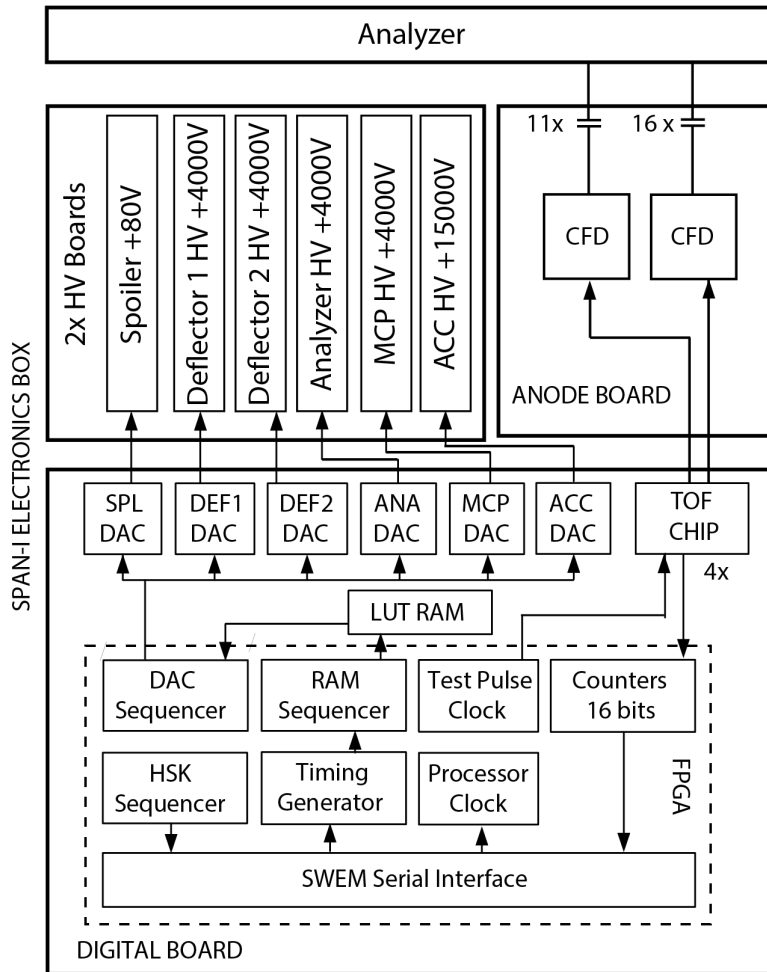


**Figure 3.** Block diagram of the SPAN-I sensor, including ESA, TOF, and individual components of the electronics box.

212 the spoiler is held at a particular voltage (maximum  
 213 of 80 V), the distribution of ions traveling through the  
 214 analyzer is reduced by electro-optically narrowing the  
 215 energy per charge passband. Initial calibration testing  
 216 has shown the spoiler to be capable of reducing the ion  
 217 flux to background levels, assuring an additional safety  
 218 mechanism for saturation of the detector. Final calibration  
 219 of the energy-dependent geometric factor are yet to  
 220 be determined. Both attenuator mechanisms are under  
 221 software control that monitors specific instrument pa-  
 222 rameters, such as counting rates and system attenuator  
 223 state. Once the count rate exceeds a preset threshold, a  
 224 set of logical and sequential combinations of the atten-  
 225 uation mechanisms are activated to maintain an ideal  
 226 count-rate. When transitioning the mechanical atten-  
 227 uator, the actuating nano-muscles require a 5 minute  
 228 relaxation time to allow for thermal settling.

#### 2.4. Time-of-Flight

229  
 230 The mechanical TOF design is a direct copy of the  
 231 TOF used on STATIC/MAVEN. The design uses two  
 232 sets of carbon foils for both the START and the STOP  
 233 signal generation, which simplifies the mechanical design  
 234 by allowing a separation of the TOF HV region (-15 kV)  
 235 from the MCP detector voltage (3 kV). In order for ions  
 236 with a mass per charge heavier than  $H^+$  and  $He^{++}$  to  
 237 penetrate two carbon foils with high enough efficiencies,  
 238 we selected ultra-thin foils ( $<1 \mu g cm^{-2}$ ) combined with  
 239 a post-acceleration voltage of -15 kV. The -15 kV TOF  
 240 HV supply also produces a secondary voltage (11/12 of  
 241 the full voltage), enabling the deflection of secondary  
 242 electrons generated by the first set of carbon foils to-  
 243 wards the START anodes below the TOF section. The  
 244 carbon foils at the entrance and exit of the TOF ana-  
 245 lyzer are additionally shielded by grids to suppress field-

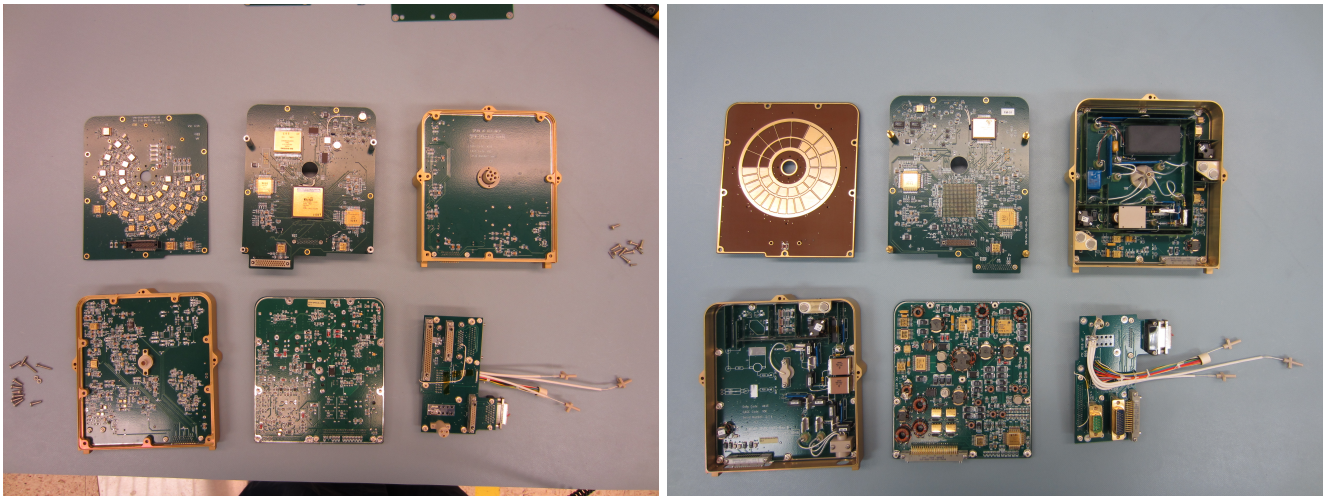


**Figure 4.** Left Figure: Backside of each individual board that is part of the electronics box. The top row shows the anode board, the digital board, and the high voltage board. the bottom row shows the second high voltage board, the low voltage power supply, and the backplane. Right figure: Front side of each individual board in the same configuration as in the figure to the left.

emissions generated by impurities and tears within the carbon foils.

ACF-Metals was the primary provider of the carbon foils. The production begins with the foils mounted on standard mica slides which were placed on top of a cantilever base and lowered into a hot-water bath containing a surfactant solution. The floating carbon foil is then retrieved by replacing the now empty glass with the stainless steel frame containing a 333 line/inch grid mesh and raising the cantilever base above the water surface. Once removed, the foils were vacuum baked and then scanned for impurities using software developed for the MAVEN mission. The selection process of the foils included a thorough review of the high resolution scans, the associated software results, and a calibration test using ion species of different mass per charge.

### 2.5. Anode Board

The SPAN-I anode board is located below a Z-Stack MCP configuration and detects the START and STOP electrons. The flight MCPs have a resistance of  $45M\Omega$  and a nominal gain of  $2 - 3 \times 10^7$ . The gain is adjustable by controlling the MCP bias voltage through software commands and is continuously monitored in flight by performing multiple MCP-Gain tests at every encounter. The electron cloud generated at the bottom of the MCP is collected by a series of 11 inner discrete anodes (STARTs) and 16 outer discrete anodes (STOPs). Each of the 27 discrete anodes is connected to a dedicated CFD located close to the anode to reduce signal travel time. The CFD enables high resolution timing-of-arrival signals independent of input pulse amplitude. The 11 inner (START) anodes have an angular

size of  $22.5^\circ$  spanning a total azimuthal FOV of  $247.5^\circ$ . The 16 outer anodes (STOPs) are separated into 10 high resolution anodes ( $11.25^\circ$ ) and 6 larger anodes ( $22.5^\circ$ ). The STOP anodes permit a finer azimuthal resolution and are aligned such that the higher resolution area is pointed towards the solar wind direction.

### 2.6. Digital Board

The SPAN-I digital board contains the main instrument field-programmable gate array (FPGA) and four individual TOF chips, each having 4 input signals from both a START and STOP CFD for a combined 16 TOF measurements. The TOF chip acquires the input signals from the CFDs and passes on the processed results to the FPGA for further analysis. The FPGA is the main processing unit of the instrument and includes functions such as command execution and science data production. It communicates directly with the SWEEP Electronics Module (SWEM), using the provided storage for data archiving and potential delivery to the spacecraft. The digital board also houses a set of MRAM and SRAM memory, where the digital-to-analogue converter (DAC) control values for the HV components, the associated sweeping tables, and data acquisition schemes are stored. More about the instrument data acquisition scheme is detailed in section 3.

### 2.7. High Voltage Power Supply Board

There are two SPAN-I high voltage power supply boards (HVPS) that operate the HV electrodes of the instrument. The first HVPS supplies high voltage to the hemisphere, spoiler, and both deflectors with voltage values controlled and set by a digital-to-analog con-

verter (DAC) chip with a 4 V reference on the digital board. The stepping, or sweeping, from one voltage value to another, occurs every 0.2 milliseconds for the full sweep (0.8 milliseconds for the targeted sweep) with a voltage settling time of <1 nanosecond. The second HVPS supplies high voltage to the MCPs and the TOF section, once again set via DACs, but held at nominal values pending further calibration. For the deflector supplies, however, the DAC is referenced relative to the hemisphere supply control voltage. Using this coupled DAC control voltage technique results in deflector biases scaled to the correct value for each hemisphere voltage step.

### 2.8. Low Voltage Power Supply Board

The LVPS generates 1.5V, 3.3V, +/- 5V, +/- 8V secondary voltages from the 22V supplied by the SWEM. As a failsafe mechanism, the 22V source is routed through the backplane to a socket with a high voltage enable plug. RIO ASIC monitors are also mounted to monitor the voltage and current draws.

### 2.9. Backplane Board

The SPAN-I backplane board has several functions: 1. Provide high voltage signals to the spoiler and deflector, 2. Transmit actuation commands to the cover mechanism and mechanical attenuator, 3. Provide access to the enable plug for ground testing and instrument safety.

## 3. MEASUREMENT OPERATIONS

### 3.1. Voltage Sweeps

SPAN-I is designed to perform a sweeping sampling of ions at a constant rate. A sweep is composed of either 1024 steps (Full) or 256 steps (Targeted), changing the instrument optics with each step by altering associated voltages and therefore sampling specific regions of phase space. There are a total of 4 sweeps that occur every 'New York' second, which is derived from a 19.2 MHz clock and subdivided into bins to form an integration time of  $2^{24}/19.2 \times 10^6$  (0.874 s). A sweep therefore happens every 218.45 ms, alternating between a Full sweep and a Targeted sweep. A Full sweep uses high volt-

age steps that allow for a coarse mapping of the entire range of the energy per charge space with the drawback of having regions where the spectrum is not sampled. This drawback is addressed with the Targeted sweep. Once the Full sweep completes, the FPGA determines which bin contained the maximum number of counts and selects the appropriate Targeted table for a high resolution scan around this region. Full sweeps contain a total of 1024 steps which are reduced to a 256 bin product by summing to every 4th step (microstepping). The Targeted sweeps do not have micro-stepping and simply step through 256 bins in the same amount of time. Figure 5 shows an example sweep of a full and targeted data acquisition modes.

### 3.2. Sweep High Voltage Look-Up Tables

Each of the 4 high voltage electrodes (hemisphere, deflectors, spoiler) sweep through voltages to sample the ambient plasma. The sweeping mechanism is controlled by the FPGA, which reads DAC values from look-up tables residing on the instrument SRAM memory and sets the voltage accordingly. There are a total of one HV look-up table (LUT) and two index LUT: the Sweep HV LUT, Full Index LUT, and Targeted Index LUT. The Sweep LUT contains the 4 DAC values for controlling the hemisphere, spoiler, deflector 1 and deflector 2. These values are all interspersed so that a reference to the start address of the first DAC setting locates the remaining three DACs. There are a total of 4096 DAC values, 16 bits long, for each of the four electrodes. The Sweep-LUT is referenced with two tables, the Full-LUT and the Targeted-LUT, that contain the correct indexes to perform a 'coarse' and 'targeted' measurement, respectively. The Full-LUT contains 1024 index values for the 1024 steps it sweeps through during a single cycle, with a micro-stepping feature that reduces the product to 256 bins by summing every 4th step. The Targeted-LUT, on the other hand, contains 256 index values for the 256 steps it sweeps through during a targeted sweep cycle. Targeted sweeps focus around the previous high voltage step where the peak counts occurred. Therefore, there are 256 separate tables of 256 indexes in the Targeted-LUT based on the 256 steps where the peak can occur.

**Table 1.** SPAN-I Instrument Design Parameters

Parameter	Value	Comments
$\Delta R/R$	0.033	Toroidal Top-Hat <sup>a</sup>
Analyzer Radii	R1 = 3.34 cm	Inner Hemisphere Toroidal Radius
	R2 = R1 * 1.030 = 3.440 cm	Outer Hemisphere Toroidal Radius
	R3 = R1 * 1.639 = 5.474 cm	Inner Hemisphere Spherical Radius
	R4 = R3 * 1.060 = 5.803 cm	Outer Hemisphere Spherical Radius
	RD = 3.863 cm	Deflector Spherical Radius
Opening Angle Hemisphere	13°	
Opening Angle Top Cap	12°	
Analyzer Constant	16.7	As derived from the optics model
Analyzer voltage (max)	0 V to 4000 V	Controllable to less than a Volt
Deflector Voltage	0 V to 4000 V	Controllable to less than a Volt
Spoiler Voltage	0 V to 80 V	Set to zero by default (no attenuation)
Energy Range	2eV to 30keV	
Analyzer energy resolution	7%	
Spoiler Attenuation Factor	10 <sup>b</sup>	Setting for E1 & E2; varies w/ energy channel
Post Analyzer Acceleration	-15kV	
Carbon Foil Thickness	<1.5 $\mu\text{g}/\text{cm}^2$	Differs for each anode
Carbon Foil Grid Frames	333 lines/inch	62% transmission
TOF gap between START/STOP	2 cm	
Thick Foil	500 nm Kapton	50 nm Al coating
Carbon Foil START Efficiency	50%	
Carbon Foil STOP Efficiency	23%	
Energy sweep rate	32 steps in 0.218 sec	
Deflector sweep rate	8 steps / 32 “microsteps” in 6.80 ms	“Microsteps” in full sweeps only
Spoiler sweep rate	32 steps in 0.218 sec	Only when enabled - zero by default
Azimuth range	247.5°	
Instantaneous field of view	247.5° × 3.507°	$\theta = 0^\circ$ (no deflection)
Field of view each sweep	247.5° × 120°	FOV blockage varies by sensor
Anode angle resolution	11.25° or 22.5°	10 Small STOPs - 6 large STOPs - 11 Large STARTs
Analyzer geometric factor	0.00105 cm <sup>2</sup> sr E	Simulations for 247.5° analyzer only
	5.984 × 10 <sup>-4</sup> cm <sup>2</sup> sr E	Including 5 × 90% transparency grids
Measurement Cadence	0.435 sec	For either Full or Targeted Sweeps (not both)
Measurement Duration	0.218 sec	For 32 energy by 8 deflector bins
Counter readout	0.852 ms	32 energy by 8 deflector bins per sweep

<sup>a</sup>Note that values in the above table are as designed values; final calibrated values to be included in a future SPAN-I calibration special issue paper.

<sup>b</sup>Estimated, final calibration pending spoiler use in Encounter 3 and beyond.

### 3.3. TOF Operations

The TOF measures the time between START and STOP pulses from a single anode for a particular an-

gle and energy per charge. The value measured is originally a value between 0 and 2047 representing the delays of 0 to 208.33 ns. Each count of the output represents 101.725 ps in delay, such that a value of 512 from the TOF converts to a value of 52.1 ns in delay. Be-

392

393

394

395

396

397

398

399

400 fore the TOF value is passed onto the data processing  
 401 unit the FPGA either accepts the 9 most significant bits  
 402 (MSBs) of the TOF, discarding the 2 least significant  
 403 bits (LSBs), or it compresses the 10 MSB into 9 bits  
 404 (discarding the LSB). The compression scheme is N for  
 405 counts less than 256, N/2+128 for counts between 256  
 406 and 511, and N/4+256 for counts greater than 511. This  
 407 compression emphasizes TOF resolution at low TOF  
 408 values. The TOF value is further categorized into a  
 409 mass per charge value by using a mass look-up-table  
 410 (MLUT) derived from ground calibration. For each en-  
 411 ergy per charge setting the 9 bits of the compressed TOF  
 412 (cTOF) values are indexed into a 512 element table. In-  
 413 stead of using the full range of high voltage settings for  
 414 each energy per charge step(65536), the MLUT uses 128  
 415 tables based on the 7 most significant bits of the hemi-  
 416 sphere DAC. The table converts the TOF value into 64  
 417 distinct masses.

#### 418 3.4. Archive and Survey Products

419 The first step in generating science products is con-  
 420 verting the time of flight measurement to a mass per  
 421 charge. Ions entering SPAN-I are first filtered by their  
 422 energy per charge, meaning that the particle travel time  
 423 will change for each energy step across the 2 cm TOF  
 424 gap. For each energy per charge setting, a separate  
 425 look-up table is used to convert the particles time-of-  
 426 flight into one of 64 distinct mass per charge values.  
 427 The next table, the Mass-Range-LUT, categorizes the  
 428 64 mass bins into 4 separate mass products defined as:

429 0-Protons, 1-Alphas, 2-Higher M/Q, 3-Background. Fi-  
 430 nally, after the particle mass is categorized into a mass  
 431 range, the FPGA will use a Mass-Bins-LUT to deter-  
 432 mine how much mass resolution to keep for each ion  
 433 product. The result is an address space in memory  
 434 defining a specific ion mass that will be filled with the  
 435 appropriate science values.

436 The second step converts the high voltage steps (En-  
 437 ergy and Elevation), the anode number (Azimuth), and  
 438 the product number (Mass Address) into an address to  
 439 increment and be filled with count measurements. The  
 440 resulting products are then summed over a programmed  
 441 number of sweeps (either all Full sweeps or all Targeted  
 442 sweeps) defined in a Sum-LUT table that holds the ex-  
 443 ponent (n) of a  $2^n$  value.

#### 444 3.5. Single Measurement

445 The SPAN-I analyzer performs a single high voltage  
 446 sweep in 0.248 s, during which a set of voltages are ap-  
 447 plied to the hemisphere, deflectors, and spoiler based on  
 448 a sweep lookup table. The first step within the sweep  
 449 sets the hemisphere voltage to its highest value and sub-  
 450 sequently steps through the remaining 31 values loga-  
 451 rithmically towards the lowest voltage. For each hemi-  
 452 sphere step, the deflectors are stepped through a series  
 453 of voltages in order to scan in elevation for a specific  
 454 energy per charge. Lastly, a spoiler voltage is set for  
 455 each hemisphere step in order to reduce the total flux of  
 456 incoming particles.

Table 2. SPAN-I Instrument Sweep Modes for Encounters 1 & 2

Mode Name	When Used	Energy Range	# Energy Steps	# Deflector Steps	# Anodes
Nominal	Encounter 1	500eV-2keV	32	8 <sup>a</sup>	8
Nominal	Encounters 2 & 3	125eV-20keV	32	8 <sup>a</sup>	8

<sup>a</sup>Sweep tables used in Encounters 1 & 2 included pre-launch deflector values, and as a result the outermost deflection angles in SPAN-I data are unreliable.

Table 3. SPAN-I Data Acquisition Modes from Encounters 1 & 2: Level 1 & 2 Data

Data Type <sup>a</sup>	When Used	Product Type	Product Name	Cadence (sec)	Anode Bins	Deflection Bins	Energy Bins
SF00	Encounter 1	Proton 3D Spectra	8D×32E×8A	27.96	8	8	32

Table 3 continued

Table 3 (continued)

Data Type <sup>a</sup>	When Used	Product Type	Product Name	Cadence (sec)	Anode Bins	Deflection Bins	Energy Bins
SF01	Encounter 1	Alpha 3D Spectra	8D×32E×8A	55.92	8	8	32
SF20	(Diagnostic)	Proton 3D Spectra	32E×64M	6.99	-	-	32
SF21	(Diagnostic)	Alpha 3D Spectra	32E×64M	13.98	-	-	32
AF00	Encounter 1	Proton 3D Spectra	8D×32E×8A	1.75	8	8	32
AF01	Encounter 1	Alpha 3D Spectra	8D×32E×8A	1.75	8	8	32
AF20	(Diagnostic)	Proton 3D Spectra	32E×64M	1.75	-	-	32
AF21	(Diagnostic)	Alpha 3D Spectra	32E×64M	1.75	-	-	32
SF00	Encounter 2	Proton 3D Spectra	8D×32E×8A	6.99	8	8	32
SF01	Encounter 2	Alpha 3D Spectra	8D×32E×8A	13.98	8	8	32
SF20	(Diagnostic)	Proton 3D Spectra	32E×64M	13.98	-	-	32
SF21	(Diagnostic)	Alpha 3D Spectra	32E×64M	13.98	-	-	32
AF00	Encounter 2	Proton 3D Spectra	8D×32E×8A	0.87	8	8	32
AF01	Encounter 2	Alpha 3D Spectra	8D×32E×8A	0.87	8	8	32
AF20	(Diagnostic)	Proton 3D Spectra	32E×64M	1.75	-	-	32
AF21	(Diagnostic)	Alpha 3D Spectra	32E×64M	1.75	-	-	32

<sup>a</sup>Targeted sweep products are not included in this table, but have identical formats to their full counterparts; “SF0” is a “Full” energy range product, and “ST0” is its “Targeted” range counterpart

<sup>b</sup>“S” stands for “Survey”, “A” stands for “Archive”, “F” stands for “Full”, “T” stands for “Targeted”.

480 efficiencies for STOP and START signals overlaid. Carbon  
481 foil efficiencies are derived from the following equation:

$$Start_{eff} = (ValidRate)/(StopRate)$$

$$Stop_{eff} = (ValidRate)/(StartRate)$$

483 where  $START_{eff}$  ( $STOP_{eff}$ ) is the START (STOP)  
484 efficiency,  $ValidRate$  is the valid events rate, and the  
485  $StartRate$  ( $StopRate$ ) is the valid START (STOP) rate.  
486 The results show a fairly consistent carbon foil efficiency  
487 for both the START ( 50%) and STOP ( 23%) across all  
488 anodes. At the edge of each anode pair is a slight drop  
489 for both efficiencies due in part to the aforementioned  
490 cross talk and grids within the TOF section that are  
491 in the sensor’s FOV. Cosmic rays and radioactive decay  
492 background is found to be minimal due to coincidence  
493 measurements with ion fluxes as high as 20 kHz.

494 In order to avoid ion feedback and to improve the  
495 signal, a 500 nm Kapton thick foil was included af-  
496 ter the second set of thin carbon foils. Ions that have  
497 passed through both thin carbon foils with an energy  
498 of >15keV are stopped by the thick foil, whereas sec-  
499 ondary electrons pass through almost unhindered. The  
500 improved signal comes from the scattering of the sec-  
501 ondary electrons themselves as the pass through the  
502 thick foil, where the narrow beam is now spread over

## 4. GROUND CALIBRATION

### 4.1. Analyzer Response and TOF Efficiencies

457  
458  
459 A slow rotation scan is performed across all 16 an-  
460 odes with a 1 keV residual gas beam and -15 kV TOF  
461 acceleration. This is to test the azimuthal analyzer re-  
462 sponse and the associated START and STOP carbon  
463 foil efficiencies, which are a measure of the carbon foil  
464 secondary electron production efficiency as a function  
465 of ion mass . Multiplying the START and STOP ef-  
466 ficiency yields a measure of the total efficiency of the  
467 TOF section. The analyzer response function for each  
468 individual anode is shown in figure 6 on the left. The  
469 anodes are drawn proportional to one another, but not  
470 to scale, and the normalized calibration measurements  
471 overlay the corresponding azimuthal angles. For larger  
472 anodes 22.5° (10-15) the relative efficiency is close to  
473 90 % with 5% cross-talk interference between adjacent  
474 anodes. For the smaller STOP anodes of 11.25° (0-9) a  
475 start anode of 22.5° is shared and the signal is divided  
476 into its separate components. In this case, the cross-talk  
477 between anodes is larger and closer to 30% while the  
478 relative efficiency stays high. The right side of figure 6  
479 shows the same anode configuration with carbon foil effi-

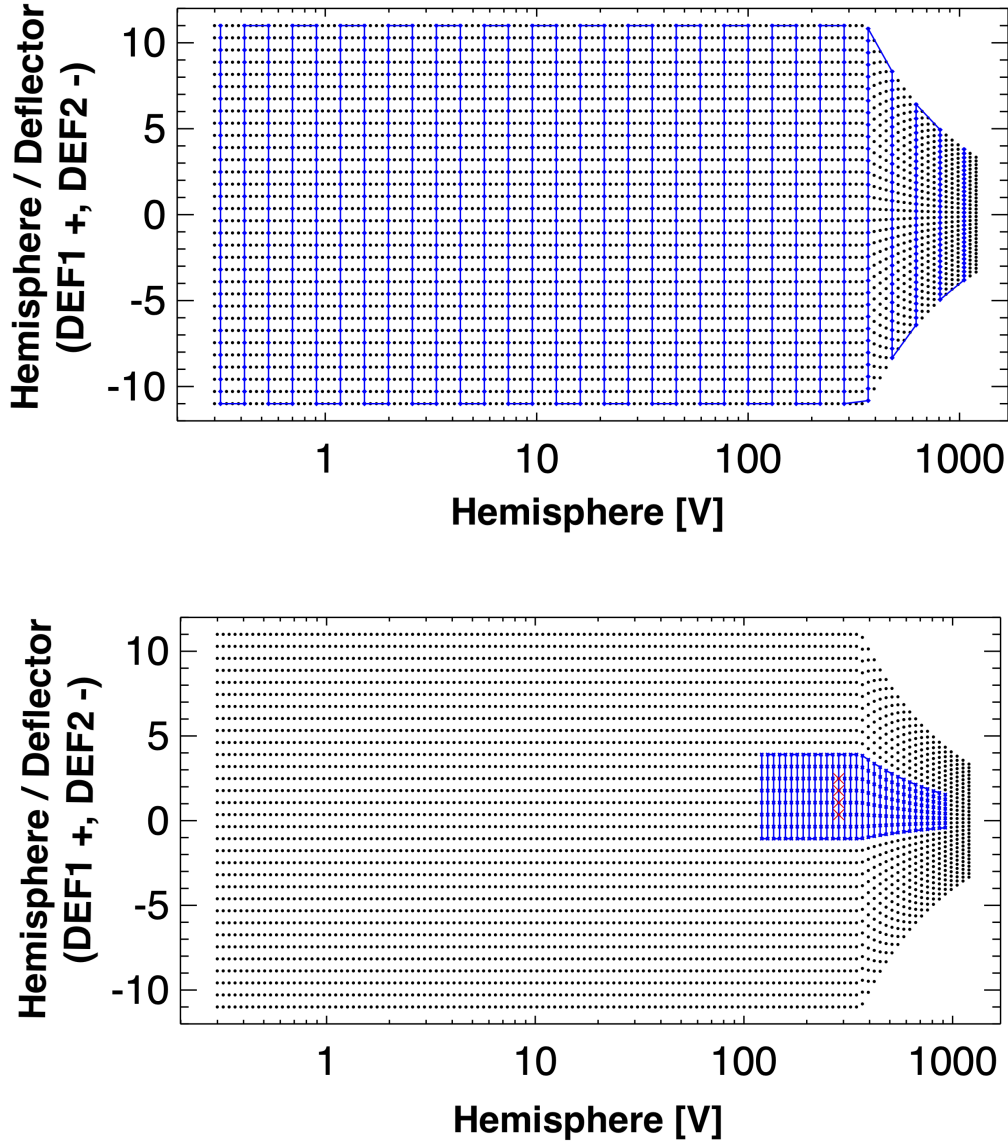


**Figure 5.** Sample sweep diagram for a full (top) and subsequent targeted (bottom) sweep. The black circles represent 4096 possible combinations of the hemisphere and both deflectors settings. The blue line shows the path that the sweep takes, beginning with deflector voltages (and microstepping) and then stepping by hemisphere voltage. Once the full/coarse sweep is complete, a targeted sweep around the peak value (in this case red crosses) is performed.

503 a greater area on the MCP and therefore reduce MCP  
504 droop.

505 The secondary electron yields of protons and helium  
506 are estimated to be 2 electrons from the thin carbon  
507 foils (Goruganthu & Wilson 1984; Ritzau & Baragiola  
508 1998). Higher masses, with the same acceleration po-  
509 tential, will typically yield higher numbers of secondary  
510 electrons. A more detailed discussion can be found in  
511 McFadden et al. (2015). More calibration of efficiencies  
512 for different mass species and acceleration will follow in  
513 order to improve Venus flybys.

#### 514 4.2. Analyzer Concentricity

515 The analyzer concentricity is verified using a series of  
516 energy scans for each anode separately. Figure 7 shows  
517 test results for anodes 0-3, with the analyzer sweeping  
518 logarithmically from 5 eV - 20 keV in order to verify the  
519 peak tracking mechanism for large energy steps in the  
520 full sweep. The top panel represents the targeted scan  
521 with peak tracking enabled, while the bottom panel rep-  
522 resents the full sweep. Both panels show a clear track-  
523 ing of the energy beam, even during instances when the  
524 beam energy was in between two full sweep energy bins.

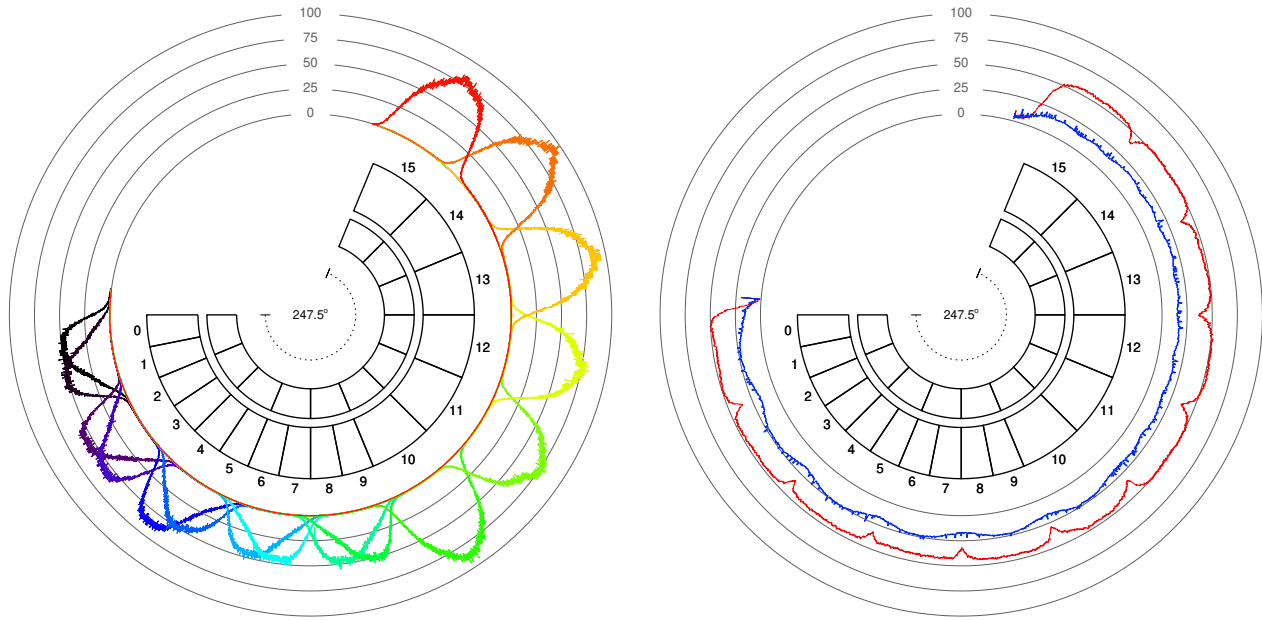


**Figure 6.** Left: Normalized instrument response function for each anode, where both the START and STOP anodes are displayed. STOP anodes 0-9 are paired with a single START anode in order to increase angular resolution. For higher resolution anodes, the effects of cross-talk are enhanced relative to the larger anodes. Right: START (red) and STOP (blue) TOF efficiencies for all anodes.

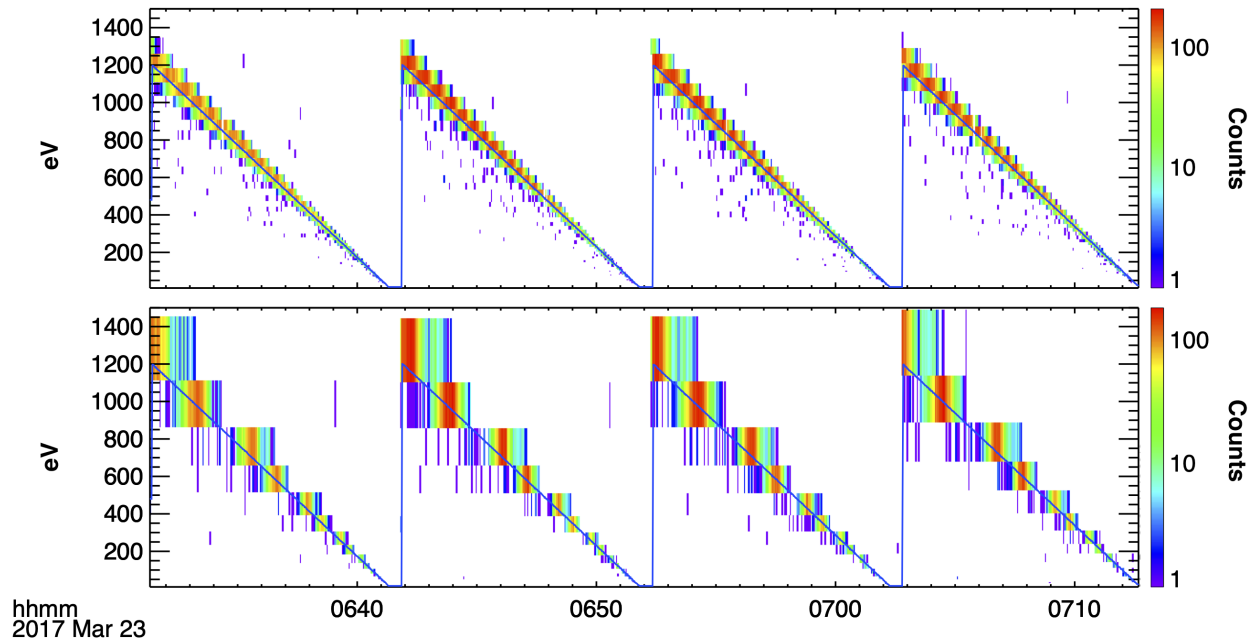


**Figure 7.** Energy scan of four individual anodes. Ion gun energies are swept from 1200 eV down to zero while the instrument sweeps in energy logarithmically from 5 eV to 20 keV. The ion gun energy is overplotted in blue. Top: Targeted product. Bottom: Full product.

525 The analyzer k-factor is derived for each anode separately and is shown in Figure 8. Conversion of energy  
526 bins from instrument values to physical units in eV is  
527 achieved by assuming a linear relationship between the  
528

529 hemisphere voltage and the energy of the particle (k-  
530 factor)

$$E/Q = k * V \quad (1)$$

531 The results show a consistent k-factor for the first  
 532 6 anodes that closely matches the expected simulated  
 533 value of 16.7. Anode 7-15 appear to be slightly lower in  
 534 value, highlighting a slight non-uniformity between the  
 535 two concentric plates.

#### 536 4.3. TOF Calibration

537 The TOF system is verified by testing the mass per  
 538 charge resolution of individual ion species for a series of  
 539 different energies. Figure 9 shows the ion travel time  
 540 in nanoseconds for 1 keV  $H^+$ ,  $H_2^+$ ,  $He^+$ ,  $N^+$ ,  $O^+$ ,  $Ne^+$ ,  
 541  $O_2^+$ , and  $Ar^+$ . A clear separation is visible between  $H^+$   
 542 and  $H_2^+$  by up to four orders of magnitude, where  $H_2^+$   
 543 is a proxy of  $He^{++}$  in the solar wind. The  $\frac{\Delta M}{M}$  are  
 544 measured to be 15% and 20%  $H^+$  and  $H_2^+$ , respectively.  
 545 This value slightly changes for different particle energies  
 546 and is taken into account using the mass-energy look-  
 547 up table. SPAN-I is also capable of measuring higher  
 548 mass species such as  $O^+$  and  $CO_2^+$ , which is ideal for  
 549 measuring escape ions during the Venus gravity assists.

550 In order to determine the correct ion travel time, and  
 551 therefore the true mass per charge of the particle, it  
 552 is important to include the energy loss component as  
 553 the ions traverse the carbon foil. The resulting effect  
 554 is a slower travel time and a broadening of the mass  
 555 per charge distribution of individual species, commonly  
 556 known as straggling. The peak of each distribution from  
 557 figure 9 is plotted in 10 together with the corresponding  
 558 ion mass per charge, taken from the calibration mea-  
 559 surements of the ion gun. In addition, three simulations  
 560 are plotted: 1. The red curve represents ion travel time  
 561 with no carbon foil present, 2. the blue curve is a sim-  
 562 ulation using the 'Stopping and Range of Ions in Mat-  
 563 ter' SRIM/TRIM software (Ziegler et al. 2010) using a  
 564 carbon foil thickness of  $0.5 \mu g \text{ cm}^{-2}$ , and 3. the light  
 565 blue curve is a similar SRIM/TRIM simulation using a  
 566 carbon foil thickness of  $1.5 \mu g \text{ cm}^{-2}$ . The results show  
 567 an agreement between the SPAN-I TOF Results and the  
 568 light blue results, indicating a carbon foil thickness three  
 569 times thicker than the nominal value.

#### 570 4.4. On-orbit Operation

571 Operation of SPAN-I can be divided into two main  
 572 modes based on spacecraft operations: the primary "en-  
 573 counter" phase of the orbits, which is approximately  
 574 ten days centered around PSP perihelion (variable by  
 575 orbit profile), and the rest of the orbit, hereafter called  
 576 "cruise" phase. The instrument measurement rate is  
 577 higher and uninterrupted during nominal encounter  
 578 phases as compared to cruise phases, during which the  
 579 data rate is considerably lower and the measurement  
 580 periods are interrupted by spacecraft communications,

581 power limitations, and other spacecraft critical opera-  
 582 tions. During periods of interest (e.g., Venus encoun-  
 583 ters), the sensors can be configured to collect more data  
 584 than typical outside of the encounter.

## 585 5. DATA DESCRIPTION

586 SPAN-I data products are classified according to the  
 587 level of calibration required to produce the files, and  
 588 the data type that is contained in those files, which are  
 589 classified by the type of processing required to produce  
 590 them. Data files are produced in CDF format, avail-  
 591 able at <https://sweap.cfa.harvard.edu/data>, and  
 592 archived in the SPDF.

### 593 5.1. Level 0 Data

594 Level 0 (L0) files are unprocessed files downlinked  
 595 directly from PSP through the Deep Space Network  
 596 (DSN) in their original packetized format created by the  
 597 spacecraft. Files contain a fixed volume of data, and are  
 598 named based on their date of acquisition. On their own,  
 599 Level 0 files are not useful for scientific analysis, but are  
 600 archived for troubleshooting purposes.

### 601 5.2. Level 1 Data

602 Level 1 (L1) files are converted from the binary L0  
 603 format into a format readable by a standard data pro-  
 604 cessing environment, such as IDL or Python pack-  
 605 ages. SPAN-I uses IDL routines in the data production  
 606 pipeline (depending on the instrument) to convert L0  
 607 files into L1 CDF files. To produce L1 files, minimal  
 608 processing is performed since the intention of the L1  
 609 data is to serve as an archive of the instrument perfor-  
 610 mance in its most raw state. All quantities in the CDF  
 611 files are in engineering units, e.g., particle counts per ac-  
 612 cumulation period per energy bin number, deflection bin  
 613 number, and anode number. Because of the units, L1  
 614 files are not useful for scientific analysis. The intention  
 615 behind archiving L1 files is to keep a record indepen-  
 616 dent from scientific conversions for pipeline debugging  
 617 purposes and instrument calibration consistency checks  
 618 over the course of the mission. Housekeeping values are  
 619 converted into temperatures, currents, and voltages. L1  
 620 files are available by request.

### 621 5.3. Level 2 Data

622 Level 2 (L2) data files are generated from L1 files. In-  
 623 strument units are converted into physical units. For  
 624 example, counts per accumulation period are converted  
 625 into differential energy flux as a function of energy in  
 626 electron-Volts (eV), and deflection and anode bin num-  
 627 bers into degrees in  $\phi$  or  $\theta$ . The L2 data coordinates  
 628 remain in the instrument frame of reference. Level 2  
 629 data are released to the public for scientific analysis.

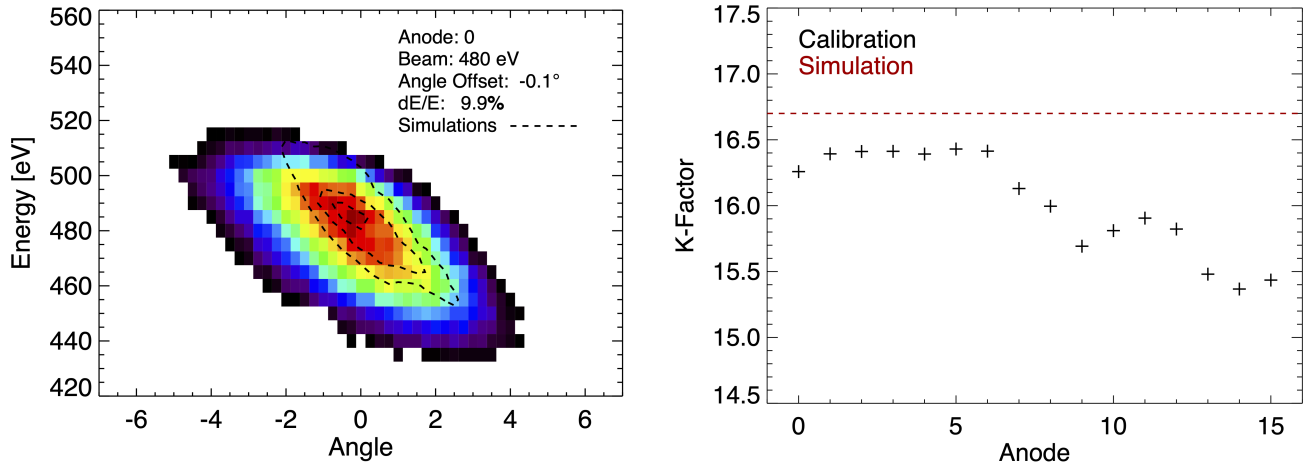


**Figure 8.** SPAN-I voltage sweep k-factor for all 16 anodes. The red dashed line represents the simulated value of 16.7.

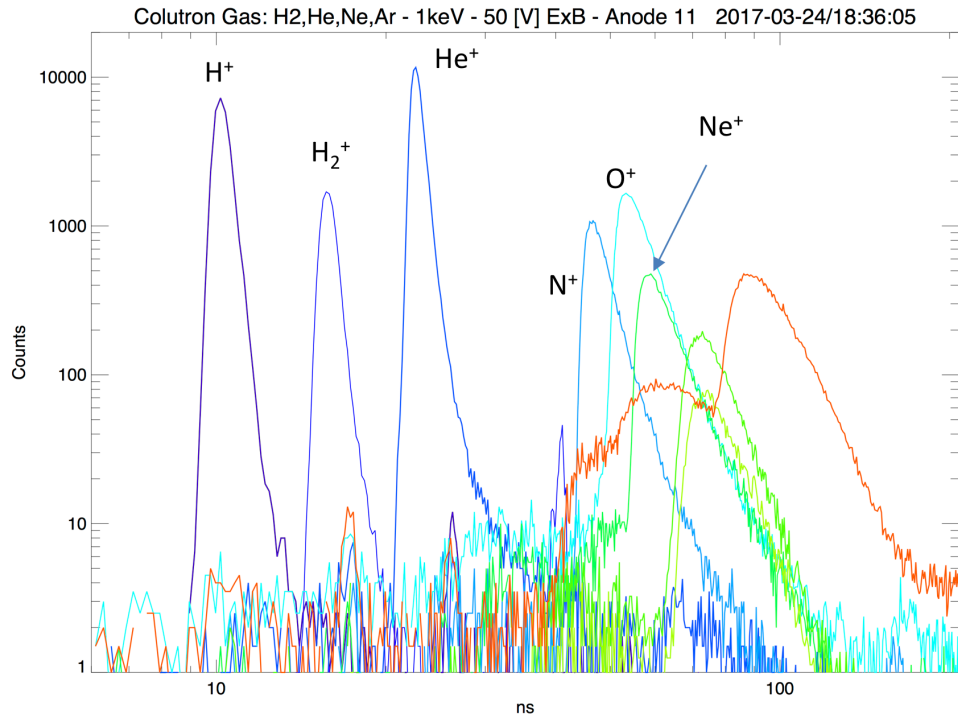


**Figure 9.** Mass per charge resolution of individual ion species obtained during ground calibration. A clear separation between H<sup>+</sup> and H<sub>2</sub><sup>+</sup> is visible by up to four orders of magnitude, which is optimal for separating the 3D velocity distribution function of the solar wind into protons ( $m/q=1$ ) and He<sup>++</sup> ( $m/q=2$ ). The TOF system is also capable of measuring higher mass species such as CO and CO<sub>2</sub>.

630

#### 5.4. Level 3 Data

631 Level 3 (L3) products are based on functions per-  
 632 formed on L2 files or other processing which expands  
 633 or reduces the number of dimensions of the L2 data set.  
 634 Ion moments and fits, which produce values of density,  
 635 temperature, and velocity, are classified as an L3 prod-  
 636 uct since they are a combination of modified L2 data.

637

#### 6. ENCOUNTER 1 AND 2

638 Parker Solar Probe successfully finished the first two  
 639 periapsis passes on November 30th 2018 and April 4th  
 640 2019, including a Venus gravity assist. The first en-  
 641 counter used an energy sweep table that ranged from 1  
 642 keV to 4 keV. We intended to use a sweep table rang-  
 643 ing from 125 eV to 20 keV to better capture the solar

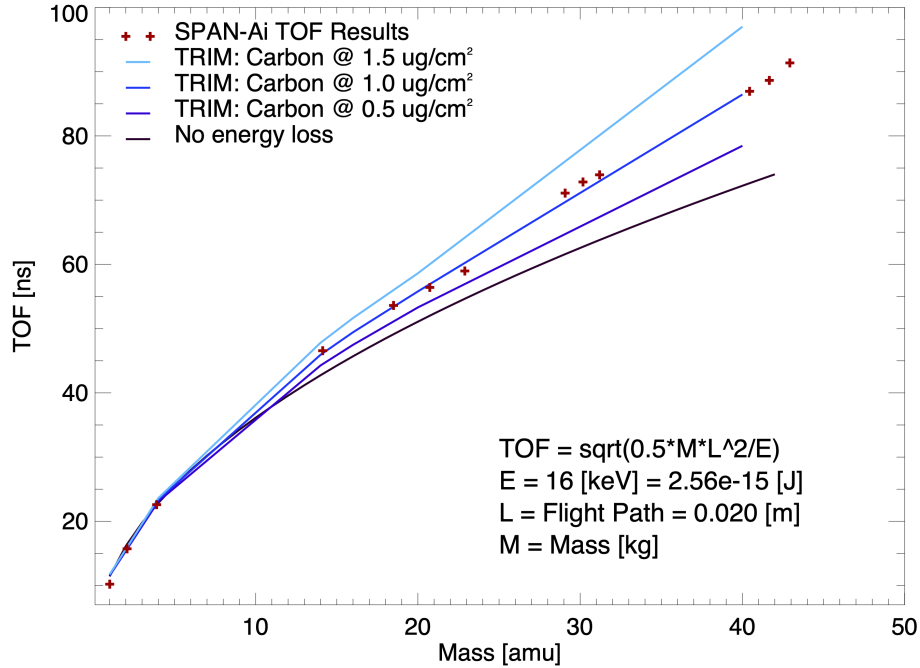


**Figure 10.** Ion travel time over the 2 cm TOF gap with an energy of 1 keV taken from ground calibration. In addition, two SRIM/TRIM simulations are presented: 1. Travel time after 1 keV particles travel a carbon foil thickness of  $0.5 \mu\text{g}/\text{cm}^2$  (purple), and carbon foil thickness of  $1.5 \mu\text{g}/\text{cm}^2$  (light blue). Travel time with no carbon foils is presented in red. Results from calibration (green) match a thickness of  $1.5 \mu\text{g}/\text{cm}^2$ .

644 wind, but due to the discovery of a corrupted sweep table,  
 645 a backup mode had to be initiated (see 7.2 for more  
 646 detail). Prior to encounter 2, new energy sweep tables  
 647 were uplinked to the spacecraft that set the instrument  
 648 energy sweep range from 125 eV - 20 keV. A summary  
 649 of the instrument configurations and product generation  
 650 are shown in tables 2 and 3

### 651 6.1. Encounter 2: Protons

652 Figure 11 shows proton measurements for all of en-  
 653 counter 2. The top panel shows the differential en-  
 654 ergy flux spectrogram of  $\text{H}^+$  ions summed over all FOV  
 655 angles. The second panel shows proton measurements  
 656 along the elevation angle of the instrument (deflectors)  
 657 summed over energy per charge and azimuth. The pro-  
 658 ton flux is clearly centered around  $0^\circ$  corresponding to  
 659 a plane that aligns with the sun-line. The third panel  
 660 shows the azimuthal FOV of the instrument, where each  
 661 bin represents a small ( $11.25^\circ$ ) or large anode ( $22.5^\circ$ ).  
 662 Anode 0 is currently not included due to its par-  
 663 tial obstruction by the thermal protection shield (TPS).  
 664 The angle range from  $168.75^\circ$  -  $180^\circ$ ) requires additional

665 flight-calibration in order to determine the correct flux.  
 666 The last panel shows distance from the sun in million  
 667 km.

668 The 3D VDFs produced by SPAN-I are akin to the  
 669 ones reported in Marsch et al. (1982), who showcased  
 670 field-aligned proton beams measured by Helios. Fig-  
 671 ure 2 of Verniero et al. (2020) similarly demonstrated  
 672 the evolution of a proton beam during an ion-scale  
 673 wave storm from Encounter 2. A single timeslice, 2019-  
 674 04-05/19:54:20, from that event is shown in figure 12  
 675 (adapted from Fig. 2(e) of Verniero et al. (2020)). The  
 676 left panel shows individual energy sweeps for each an-  
 677 ode and deflection combination plotted separately with  
 678 the Alfvén velocity overplotted with a black dashed line.  
 679 The middle and right panels of figure 12 represent 2D  
 680 contour elevations sliced through the  $\phi$  and  $\theta$  plane,  
 681 respectively. The black arrow shows the orientation of  
 682 the magnetic field, where the length of the arrow is the  
 683 Alfvén speed and the head is placed at the SPC mea-  
 684 sured solar wind velocity. Here, we are referring to the  
 685 Alfvén speed of the total proton distribution. Two sep-

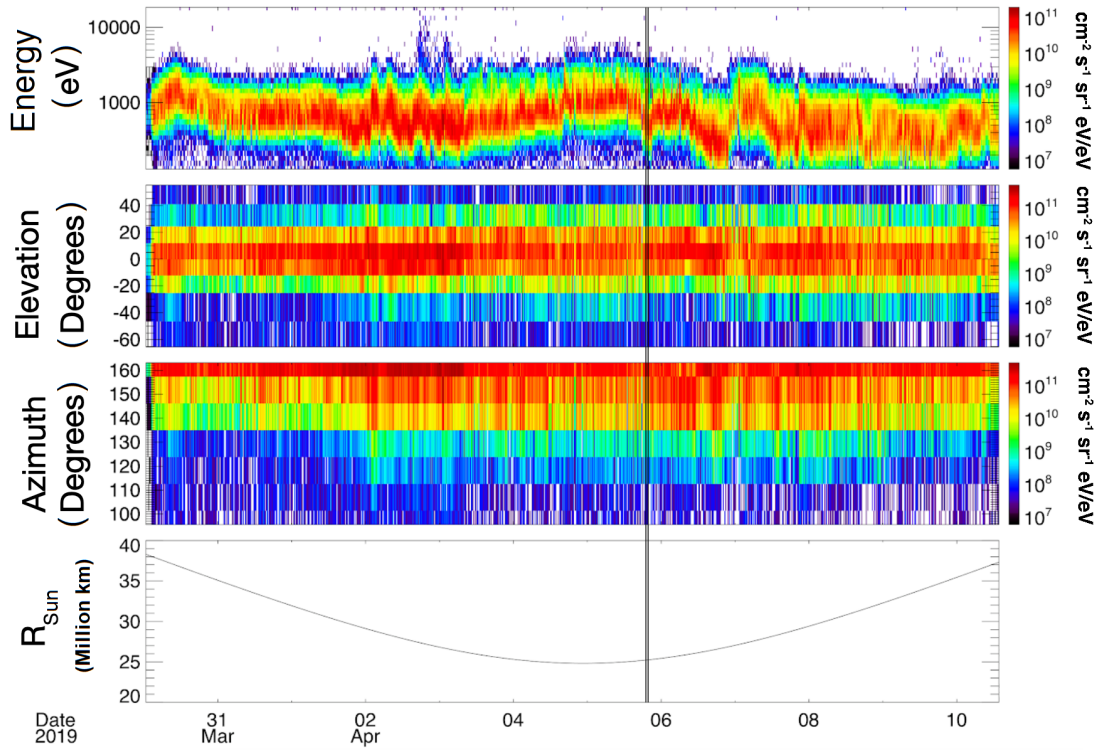


**Figure 11.** Proton measurements for all of encounter 2. The top panel shows the energy per charge summed over all look directions, the second panel shows the flux in elevation (deflector sweep), the third panel shows the azimuthal flux (anodes), and the last panel shows the distance from the sun in Million km. The vertical black line marks the time of the data presented in Figure 12.

686 arate proton distributions are clearly visible: the core  
 687 and the beam. Following the convention discussed in  
 688 Verniero et al. (2020), the “core” is defined as the popu-  
 689 lation centered around the peak in phase space density,  
 690 while the “beam” component comprises the tail.

691 The middle panel of figure 12 illustrates how much of  
 692 the proton distribution lies in SPAN-I’s FOV; in this  
 693 particular timeslice, we see that the core is partially  
 694 visible. The 2D cut through the  $\theta$  plane, in the right  
 695 panel of figure 12, reveals a dramatic field-aligned beam  
 696 featuring a separate peak (green) that is markedly dis-  
 697 tinct from the core. The left panel of figure 12 shows  
 698 that the beam well-surpasses the Alfvén speed. Pre-  
 699 vious observations of VDFs featuring differential flows  
 700 between different ion populations (Feldman et al. 1973,  
 701 1974; Marsch et al. 1982; Marsch & Livi 1987; Neuge-  
 702 bauer et al. 1996; Steinberg et al. 1996; Kasper et al.  
 703 2006; Podesta & Gary 2011) are known to drive the  
 704 VDFs unstable, subsequently leading to wave genera-  
 705 tion (Daughton & Gary 1998; Hu & Habbal 1999; Gary  
 706 et al. 2000; Marsch 2006; Maneva et al. 2013; Verscharen  
 707 & Chandran 2013; Verscharen et al. 2013). The prelim-  
 708 inary instability analysis conducted by Verniero et al.  
 709 (2020) underscores the ability for SPAN-I data prod-  
 710 ucts to study fundamental processes that govern energy  
 711 transfer mechanisms in the solar wind, such as wave-  
 712 particle interactions.

713 Based on ground calibration, the beam measurement  
 714 is completely unaffected by the presence of alpha parti-  
 715 cles at that same energy and are thus resolved without  
 716 interference. Throughout the encounter, the appearance  
 717 and disappearance of the proton beam can be attributed  
 718 to the limited FOV of the instrument, hence the addi-  
 719 tional presence of SPC.

## 6.2. Encounter 2: Alphas

720  
 721  $\text{He}^{++}$  measurements can be see in Figure 13. For com-  
 722 parison, the first panel shows the proton spectrogram  
 723 for encounter 2. The second panel shows the  $\text{He}^{++}$  dif-  
 724 ferential energy flux spectrogram, once again summed  
 725 over all FOV angles. A clear proton contamination is  
 726 visible within the data that appears below the  $\text{He}^{++}$   
 727 distribution. In additiona, the highest energy bin con-  
 728 tains counts from the energy sweep retrace as the in-  
 729 strument does not engage a deadtime during the cyc-  
 730 cling of the voltage table. Roughly 1% of protons leak  
 731 into the  $\text{He}^{++}$  mass channel and present a large enough  
 732 contamination that matches the density of  $\text{He}^{++}$ . This  
 733 issue is addressed by taking the proton channel and sub-  
 734 tracting a time-varying percentage of the flux from the  
 735  $\text{He}^{++}$  channel. The bottom panel of Figure 13 shows  
 736 the results of the subtraction algorithm performed on

737 encounter 2. The proton contamination is greatly re-  
 738 duced and the  $\text{He}^{++}$  distribution becomes apparent.

## 7. INSTRUMENT CAVEATS

### 7.1. Partial 3D Distribution function

741 SPAN-I is located behind PSP’s Thermal Protection  
 742 Shield (TPS) and can only observe the partial distribu-  
 743 tion function of the solar wind. The first  $8^\circ$  closest to  
 744 the spacecraft z-axis are completely obstructed, mean-  
 745 ing that anode 0, which has a  $11.25^\circ$  azimuthal size,  
 746 is 70% covered. For encounters 1 and 2 the the in-  
 747 strument mostly measured the wings of the solar wind  
 748 distribution function, with occasional intervals when the  
 749 full distribution was visible.

### 7.2. Table Corruption

751 During first turn on, it was discovered that one of  
 752 the instrument sweep tables was corrupted. This was  
 753 evidenced by the fast housekeeping, which monitors the  
 754 HV supply, and the resulting failed checksum. This issue  
 755 was immediately addressed by selecting a backup table  
 756 to avoid a total loss of data for the first encounter. The  
 757 backup table has an energy range from 1 keV - 4 keV,  
 758 resulting in the solar wind beam flowing in and out of  
 759 the instrument energy range.

### 7.3. Limited Commissioning Time

760  
 761 Commissioning of SPAN-I, including its configuration  
 762 and HV ramping, was limited in time due to spacecraft  
 763 maneuvers that placed the sun behind the heat shield  
 764 closely after launch and therefore out of the FOV. The  
 765 spacecraft did perform a transient slew in order to obtain  
 766 the solar wind into the FOV of SPAN-I, which lasted 20  
 767 minutes. The test was used to confirm full functionality  
 768 of the instrument.

### 7.4. Protons Bleeding into Alpha Channel

770 When ions travel through the TOF they initially col-  
 771 lide with the first set of carbon foils that generate the  
 772 START signal. The interaction with the carbon foil  
 773 causes a slight loss in kinetic energy; therefore, ions are  
 774 measured to travel slower than their expected velocity.  
 775 This straggling effect is especially noticeable in high flux  
 776 beams such as Protons, to the point that enough energy  
 777 is lost to appear within the Alpha product. This issue  
 778 is addressed for the Alpha channel by subtracting a per-  
 779 centage of the proton channel, since straggling protons  
 780 appear at the same energy per charge in both channels.

### 7.5. Constant Background and Ghost Peaks

781  
 782 Part of the background that is being measured by the  
 783 sensor originates within the MCPs, such as radioactive

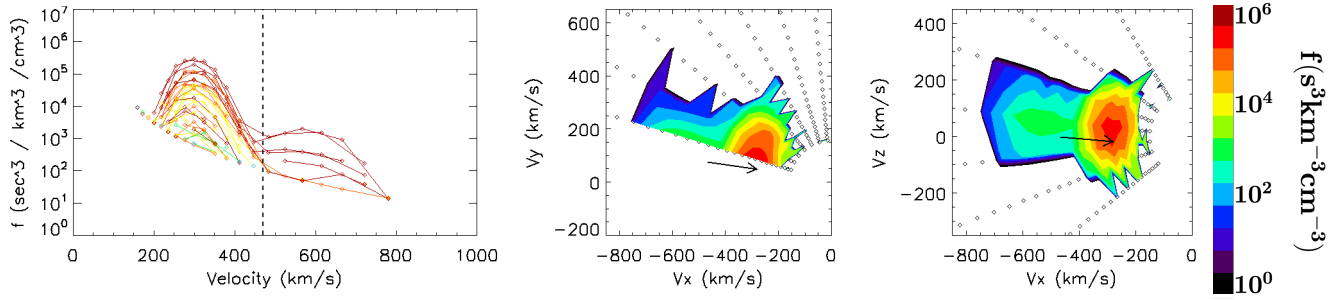


**Figure 12.** VDFs from 2019-04-05/19:54:20 showing the core at 350 km/s and the beam 600 km/s, without any interference from  $\text{He}^{++}$ . Left: Phase space density of  $\text{H}^+$  for all look directions. The black dashed line represents the Alfvén velocity. Middle: Contour elevations showing a 2D slice through the  $\phi$  plane. Right: Contour elevations showing a 2D slice through the  $\theta$  plane. The black arrow represents the magnetic field direction in SPAN-I coordinates, where the head is at the solar wind velocity (measured by SPC) and the length is the Alfvén speed. Note that this figure is from the same time period shown in Fig. 2e of Verniero et al. (2020), which illustrated the evolution of a proton beam simultaneous with an ion-scale wave storm in Encounter 2.

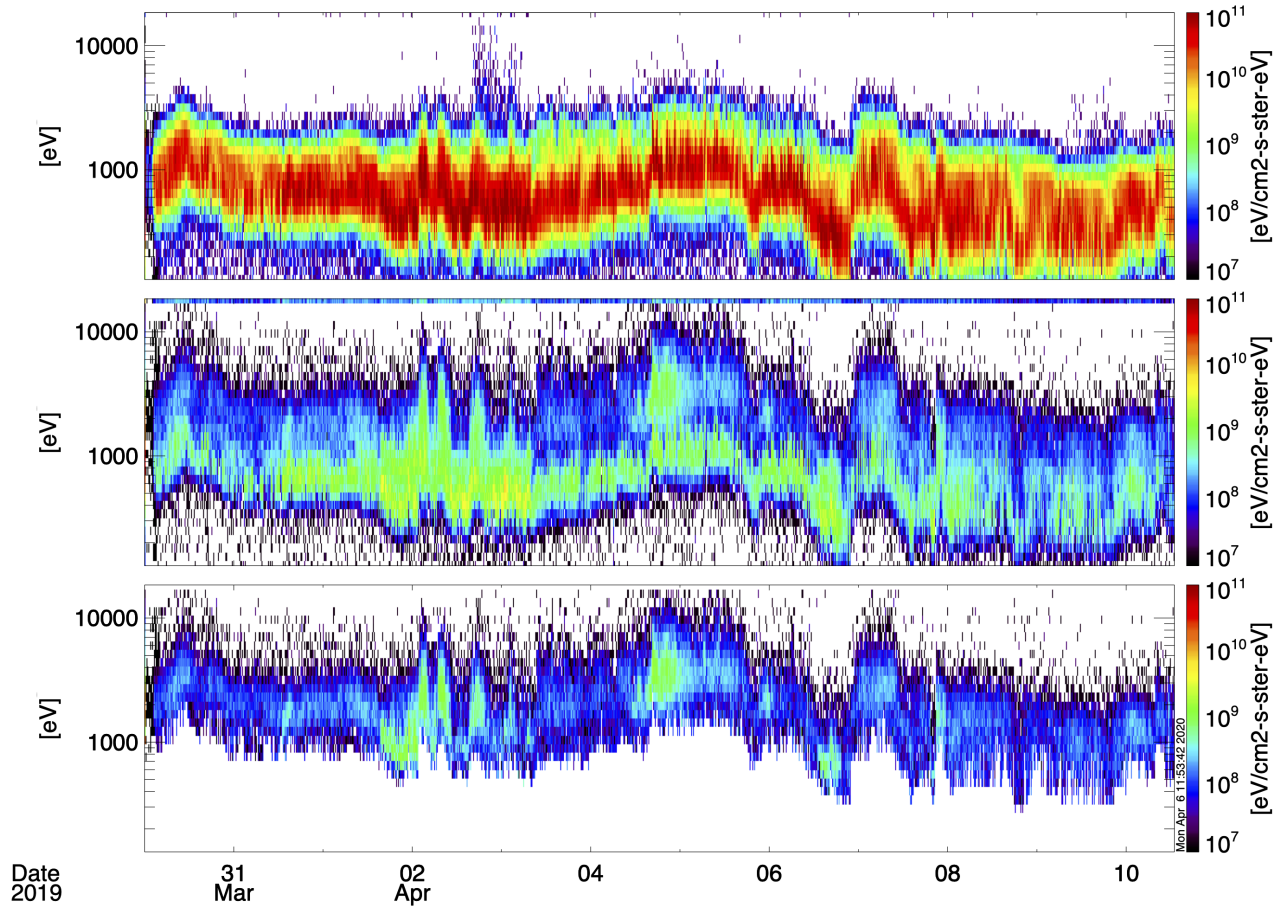


**Figure 13.** Energy spectrogram of protons (top), alphas (middle), and alphas corrected for proton bleeding (bottom). Separation between protons and alphas allows for the first individual measurements of the 3D distribution functions of  $\text{H}^+$  and  $\text{He}^{++}$  in the inner heliosphere.

784 decay of the glass and cosmic ray penetration. This  
 785 background was at most 10 Hz and does not signifi-  
 786 cantly contribute to the overall valid events. Another  
 787 source of constant background comes from coincidence  
 788 measurements, where the START and STOP pulses are  
 789 triggered by two different ions. This has been found to  
 790 be on the order of 1% for fluxes 100 kHz and scales up  
 791 for larger fluxes (McFadden et al. 2015).

792 Deviations from the nominal mass peak can occur due  
 793 to interactions between ions and the carbon foils. Ghost  
 794 peaks are generally caused by a delay of a START or  
 795 STOP signals due to the finite probability of particles  
 796 penetrating the carbon foil of <30%. Ions that pass  
 797 through the foil can emerge as neutrals 90% of the time.  
 798 If ions emerges with a positive charge they can reflect  
 799 back to the carbon foils and generate a delayed sec-  
 800 ondary electron, and therefore a delayed time-of-flight  
 801 measurement.

### 802 7.6. High Voltage Sweep Hysteresis

803 The high voltage sweeps are arranged such that the  
 804 hemisphere (energy per charge) is held at a constant  
 805 voltage value (starting with the highest within the se-  
 806 ries) while the deflectors are swept in one direction (see  
 807 figure 5). When plotting individual energy spectra a clear  
 808 hysteresis is observed, where the sweeping of the deflec-  
 809 tor voltages lags and differs depending on the direction  
 810 in which it sweeps. This results in a slight offset in the  
 811 deflection angle from the predetermined table values for  
 812 alternating energy sweeps. This effect will be addressed  
 813 in future in-flight calibrations.

## 814 8. CONCLUSION

815 The SPAN-I sensor will make measurements of the so-  
 816 lar wind 3D velocity distribution function for protons,  
 817 alphas, and higher mass-per-charge species within the  
 818 inner heliosphere. Together with SPC, it will be the first  
 819 ion sensor since Helios to measure this region and further  
 820 our knowledge by making the first measurements ever in-  
 821 side of 0.29 AU. SPAN-I is a high heritage electrostatic  
 822 analyzer combined with a mass-per-charge discrimina-  
 823 tor in order to resolve the underlying physics behind  
 824 several solar wind phenomena. This includes the trac-  
 825 ing the flow of energy that accelerates the solar wind  
 826 and exploring the mechanics that transport energetic  
 827 particles. The instrument is situated on the ram side  
 828 of the spacecraft and can measure the bulk of the so-  
 829 lar wind during times of high aberration as the VDF  
 830 peak enters the instrument aperture. The energy and  
 831 deflector sweeps are arranged to capture the bulk of the  
 832 solar wind and are adjustable over the lifetime of the  
 833 mission in order to adapt to unexplored regimes. The  
 834 SPAN-I instrument together with the entire SWEAP in-  
 835 strument suite will provide the most complete coverage  
 836 of the solar wind plasma in the inner heliosphere and  
 837 will contribute to observations needed by the scientific  
 838 community to address outstanding questions of our he-  
 839 liosphere.

840 *This work was funded through work on the NASA con-*  
 841 *tract NNN06AA01C. The authors wish to acknowledge*  
 842 *the significant work of all of the engineering staff that*  
 843 *worked on the spacecraft and SPAN-Ion instrument, es-*  
 844 *pecially Chris Scholz, Matt Reinhart, Andrew Peddie,*  
 845 *Other APL folks, and Other UCB folks for their invalu-*  
 846 *able suggestions on the manuscript.*

## REFERENCES

- 847 Carlson, C. W., McFadden, J. P., Turin, P., Curtis, D. W.,  
 848 & Magoncelli, A. 2001, *Space Science Reviews*, 98, 33
- 849 Daughton, W., & Gary, P. S. 1998, *Journal of Geophysical*  
 850 *Research*, 103, 20613. <https://agupubs.onlinelibrary.wiley.com/doi/abs/10.1029/98JA01385>
- 851 Feldman, W. C., Asbridge, J. R., Bame, S. J., &  
 852 Montgomery, M. D. 1973, *Journal of Geophysical*  
 853 *Research*, 78, 2017
- 854 —. 1974, *Reviews of Geophysics and Space Physics*, 12, 715
- 855 Fox, N. J., Velli, M. C., Bale, S. D., et al. 2016, *Space*  
 856 *Science Reviews*, 1
- 857 Gary, S. P., Yin, L., Winske, D., & Reisenfeld, D. B. 2000,  
 858 *Geophysical Research Letters*, 27, 1355
- 859 Goruganthu, R. R., & Wilson, W. G. 1984, *Review of*  
 860 *Scientific Instruments*, 55, 2030
- 861 Hu, Y. Q., & Habbal, S. R. 1999, *Journal of Geophysical*  
 862 *Research*, 104, 17045
- 863 Kasper, J. C., Lazarus, A. J., Steinberg, J. T., Ogilvie,  
 864 K. W., & Szabo, A. 2006, *Journal of Geophysical*  
 865 *Research (Space Physics)*, 111, A03105
- 866 Kasper, J. C., Abiad, R., Austin, G., et al. 2015, *Space*  
 867 *Science Reviews*, 1
- 868 Klumpar, D. M., Mobius, E., Kistler, L. M., et al. 2001,  
 869 *Space Science Reviews*, 98, 197
- 870 Maneva, Y. G., ViñAs, A. F., & Ofman, L. 2013, *Journal of*  
 871 *Geophysical Research*, 118, 2842
- 872 Marsch, E. 2006, *Living Reviews in Solar Physics*, 3, 1.  
 873 <http://www.livingreviews.org/lrsp-2006-1>

- 875 Marsch, E., & Livi, S. 1987, *Journal of Geophysical*  
876 *Research*, 92, 7263. [https://agupubs.onlinelibrary.wiley.](https://agupubs.onlinelibrary.wiley.com/doi/abs/10.1029/JA092iA07p07263)  
877 [com/doi/abs/10.1029/JA092iA07p07263](https://agupubs.onlinelibrary.wiley.com/doi/abs/10.1029/JA092iA07p07263)
- 878 Marsch, E., Schwenn, R., Rosenbauer, H., et al. 1982,  
879 *Journal of Geophysical Research*, 87, 52
- 880 McFadden, J. P., Kortmann, O., Curtis, D., et al. 2015,  
881 *Space Science Reviews*, 1
- 882 Neugebauer, M., Goldstein, B. E., Smith, E. J., & Feldman,  
883 W. C. 1996, *Journal of Geophysical Research*, 101, 17047
- 884 Podesta, J. J., & Gary, S. P. 2011, *The Astrophysical*  
885 *Journal*, 742, 41
- 886 Reme, H., BOSQUED, J. M., SAUVAUD, J. A., et al. 1997,  
887 *Space Science Reviews*, 79, 303
- 888 Ritzau, S. M., & Baragiola, R. A. 1998, *Physical Review B*  
889 *(Condensed Matter and Materials Physics)*, 58, 2529
- 890 Steinberg, J. T., Lazarus, A. J., Ogilvie, K. W., Lepping,  
891 R., & Byrnes, J. 1996, *Geophysical Research Letters*, 23,  
892 1183
- 893 Verniero, J. L., Larson, D. E., Livi, R., et al. 2020, *The*  
894 *Astrophysical Journal Supplement Series*, 248, 5.  
895 <https://doi.org/10.3847/2F1538-4365%2F202007000>
- 896 Verscharen, D., Bourouaine, S., Chandran, B. D. G., &  
897 Maruca, B. A. 2013, *The Astrophysical Journal*, 773, 8
- 898 Verscharen, D., & Chandran, B. D. G. 2013, *The*  
899 *Astrophysical Journal*, 764, 88
- 900 Ziegler, J. F., Ziegler, M. D., & Biersack, J. P. 2010,  
901 *Nuclear Instruments and Methods in Physics Research*  
902 *Section B*, 268, 1818